Applied Catalysis B: Environmental 243 (2019) 195–203

Contents lists available at ScienceDirect

Applied Catalysis B: Environmental

journal homepage: www.elsevier.com/locate/apcatb

Mn- and N- doped carbon as promising catalysts for oxygen reduction reaction: Theoretical prediction and experimental validation

Kexi Liu[a,1], Zhi Qiao[b,1], Sooyeon Hwang[c], Zhenyu Liu[a], Hanguang Zhang[b], Dong Su[c], Hui Xu[d], Gang Wu[b,*], Guofeng Wang[a,*]

[a] Department o Mechanical Engineering and Materials Science, University of Pittsburgh, Pittsburgh, PA, 15261, United States
[b] Department of Chemical and Biological Engineering, University at Buffalo, the State University of New York, Buffalo, NY, 14260, United States
[c] Center for Functional Nanomaterials, Brookhaven National Laboratory, Upton, NY,11973, United States
[d] Giner Inc., Newton, MA, 02466, United States

ARTICLE INFO

Keywords:
Oxygen reduction reaction
Density functional theory
Microkinetic analysis
Mn-N_4active site
Polymer hydrogel

ABSTRACT

Development of platinum group metal (PGM)-free as well as iron-free electrocatalysts is imperative to achieve low-cost and long-term durability of polymer electrolyte membrane fuel cells. Here, we combined computational and experimental studies to investigate the mechanism, activity, and durability of Mn and N co-doped carbon (denoted as Mn-N-C) as promising catalysts for oxygen reduction reaction (ORR) in challenging acid medium. The first-principles density functional theory calculations predict that it is favorable for O_2 to be reduced into H_2O via four-electron pathway on MnN_4 sites embedded in carbon layer. Using the reaction energies calculated from DFT, microkinetic analysis predicts that the MnN_4 sites could catalyze ORR with a half-wave potential only 60 mV lower than that of Pt (111) and 80 mV lower than that of the FeN_4 sites embedded in carbon layer, assuming the same density of active sites in the catalysts. Motivated by the computational prediction, we synthesized a Mn-N-C catalyst using a polymer (i.e., polyaniline-PANI) hydrogel precursor via a high temperature approach. Structural characterization indicates that atomically dispersed Mn sites coordinated with N are very likely formed in the catalyst. Electrochemical measurements show that the synthesized Mn-N-C catalyst can promote four-electron ORR with a catalytic activity in acids comparable to that of the Fe-N-C catalyst prepared using the same procedure. More importantly, the Mn-N-C catalyst exhibits superior potential cyclic stability, only losing 20 mV after 10000 cycles (0.6 to 1.0 V in O_2 saturated electrolyte). In comparison, the Fe-N-C catalyst would loss 80 mV after only 5000 cycles under the same testing conditions. Our computational and experimental results strongly suggest that the Mn and N co-doped carbon could be promising high-performance catalysts for ORR in acidic medium.

1. Introduction

Polymer electrolyte membrane fuel cells (PEMFCs) are energy conversion technology of inherent high efficiency and environmental friendliness [1,2]. A forefront research topic of PEMFC development is to find cost-effective cathode catalysts to replace expensive platinum group metal (PGM) based catalysts for oxygen reduction reaction (ORR) in acid medium. In this regard, non-precious transition metals (e.g., Fe or Co) and nitrogen (N) co-doped carbon (denoted as M-N-C) have shown great promise as PGM-free electrocatalysts for PEMFCs [3–7]. Especially, the Fe-N-C represents the state of the art PGM-free catalyst, which has exhibited catalytic activity approaching to that of Pt/C catalysts in acids [8–10]. Consequently, the chemical nature of the active sites and the pathway of ORR on the Fe-N-C catalysts have been extensively studied [11–13]. Both X-ray absorption near edge structure [14] and aberration-corrected scanning transmission electron microscopy [15] characterization studies reveal that FeN_4 sites embedded in carbon layers are most possibly responsible for the obsereved ORR activities of the Fe-N-C catalysts.

Although the Fe-N-C catalysts demonstrate decent catalytic activity for the ORR, their stability under electrochemical oxidation environments has been found to be a big challenge compared to that of PGM catalysts. The corrosion of active sites (and/or carbon supports) and the loss of Fe species into aqueous electrolytes were reported to be the main

* Corresponding authors.
E-mail addresses: gangwu@buffalo.edu (G. Wu), guw8@pitt.edu (G. Wang).
[1] These authors contributed equally.

https://doi.org/10.1016/j.apcatb.2018.10.034
Received 7 July 2018; Received in revised form 9 October 2018; Accepted 14 October 2018
Available online 16 October 2018
0926-3373/

reasons for the activity degradation of the Fe-N-C catalysts [16,17]. Moreover, exposure to hydrogen peroxide has a detrimental effect on the long-term performance stability of PANI-derived Fe-N-C catalysts [18]. Even worse, the Fe^{2+} dissolved from the catalysts was expected to promote the decomposition of hydrogen peroxide into highly reactive free radicals, which attack the fuel cell membrane and thus can cause device failure [19]. Hence, it is necessary to develop durable, Fe-free M-N-C catalysts for PEMFCs [20].

The Co-N-C catalyst has been widely explored as a possible PGM-free and Fe-free electrocatalyst for ORR [4,21]. However, the ORR activity of Co-N-C catalyst is usually inferior to that of the Fe-N-C and it produces high yield of hydrogen peroxide in acid. To date, the best Co-N-C catalyst was shown to have a half-wave potential $E_{1/2}$ of 0.80 V and hydrogen peroxide yield of 5% [20]. The appreciable production of hydrogen peroxide indicates that some (if not all) active sites of the Co-N-C catalysts could only promote two-electron instead of the desirable four-electron ORR as the Fe-N-C catalysts do [21]. Therefore, it is of great interest to search for other PGM-free and Fe-free electrocatalysts, which are able to mainly promote four-electron ORR. Zheng et al. have evaluated the ORR activity of M-N-C catalysts with metal M being Mn, Fe, Co or Ni, and showed that Mn-N-C could exhibit reasonable ORR activity [22]. However, from a computational perspective, this previous study considered only the thermodynamics of ORR reaction and thus did not provide detailed understanding of the kinetics of ORR in these catalysts. In this study, we have performed the first-principles density functional theory (DFT) calculations and microkinetic analysis for predicting the ORR kinetic activity of MnN_4 site in a carbon layer. Furthermore, the theoretical prediction and understanding are experimentally verified through synthesizing a novel hydrogel polymer-derived Mn-N-C catalyst showing ORR activity comparable to that of the Fe-N-C catalysts. Our present study suggests that the Mn-N-C catalyst could be a promising alternative to the Fe-N-C as a PGM-free cathode for PEMFC applications.

2. Computational and expeimental methods

2.1. DFT calculation

The spin-polarized DFT calculations [23,24] were performed using the Vienna ab initio simulation package (VASP) code [25,26]. Projector augmented wave (PAW) method [27,28] was used to describe the core and valence electrons, and a plane wave basis set with a kinetic energy cutoff of 400 eV was used to expand the wavefunctions. Electronic exchange and correlation was described within the framework of generalized gradient approximation (GGA) using the revised Perdew-Burke-Ernzerhof (RPBE) functional [29]. The convergence criterion of electronic and geometry optimization was set to be $1 \times 10^{-6} eV$ for energy and $0.02\, eV/Å$ for force, respectively.

The active site of the M-N-C catalysts was modeled as a MN_4 (M = Fe or Mn) moiety embedded in a carbon layer (as shown in Fig. 1a). The Brillouin zone was sampled using a Monkhorst-pack [30] $4 \times 4 \times 1$ k-point grid for the modelled M-N-C catalysts. For comparison, we also predicted the ORR rate on Pt (111) surface. The Pt (111) surface was modeled using a three-layer slab with a rectangle cell and 3×2 atoms in each layer (as shown in Fig. 1b). The Brillouin zone was sampled using a Monkhorst-pack $4 \times 6 \times 1$ k-point grid for the Pt (111). Taking solvation effect into account, we added a layer of water molecules on the catalyst surface explicitly. The water layer consists of a two-dimensional hexagonal hydrogen bond network with one half of the water molecules lying parallel to the slab and the other half with one hydrogen pointing to the surface [31]. The transition state of elementary chemical reactions was located using the climbing image nudged elastic band (CI-NEB) method [32] with a convergence of 0.05 eV/Å for the force components both along and perpendicular to the tangent of the reaction path. The free energy of each ORR intermediate was calculated using computational hydrogen electrode method developed by Nørskov et al. [33] Using the reversible hydrogen electrode (RHE) as reference, the free energy of $H^+_{(aq)} + e^-$ can be calculated by the free energy of $\frac{1}{2}H_2$. In this work, the reaction free energy was calculated as

$$\Delta G = \Delta E + \Delta E_{ZPE} - T\Delta S + neU \quad (1)$$

In this equation, ΔE is the reaction energy calculated by DFT. In our water layer covered slab models, the solvation corrections (ΔE_{solv}) were already included in the ΔE from DFT calculations. Zero-point corrections (ΔE_{ZPE}) were calculated as $ZPE = \sum_i \frac{1}{2} h\nu_i$, where h is Planck's constant and ν_i is the frequency of the i th vibrational mode of binding molecules. $T\Delta S$ is the entropy term and neU is the potential dependent free energy shift at electrode potential U with respect to that at zero potential for a reaction obtaining n electrons. The electrode potentials (U) are given as the potential values with reference to RHE.

2.2. Microkinetic analysis

A microkinetic model [34] was developed to predict the polarization curve of the ORR catalysts using the DFT calculated free energy change ($\Delta G(U)$) and activation energy ($E_a(U)$) for all the ORR elementary steps as inputs. It notes that we have considered the variation of the reaction energies as a function of electrode potential (U) in this study. Our microkinetic model defines a set of coupled partial differential equations describing the time variation of surface ORR species from the rate equations (see Supporting Information) and the site conservation equation describing that the total site coverage is equal to one. These equations are solved numerically at the steady state where the coverage of surface ORR species becomes invariant with time. The outputs of our microkinetic model include the reaction rate for each elementary step and the total turnover frequency (TOF) of ORR on the catalysts of interest.

In our microkinetic model specifically for the ORR, four reaction pathways involving thirteen elementary reaction steps were taken into consideration. At the first step, O_2 molecules diffuse from the bulk electrolyte to the electrode-electrolyte interface,

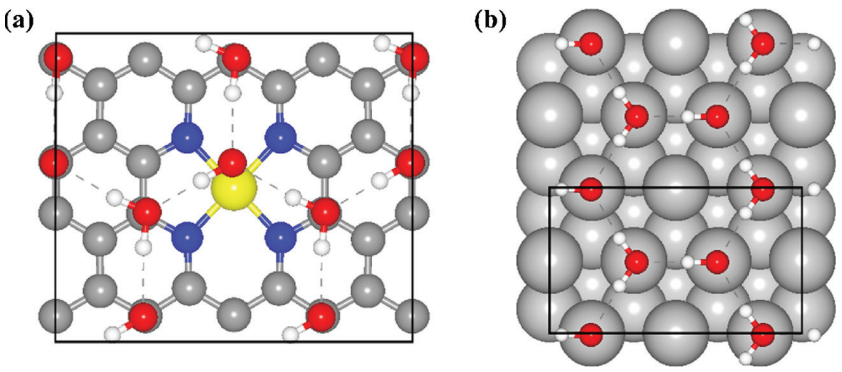

Fig. 1. Atomistic structures of our simulation models for (a) a FeN_4 or MnN_4 active site embedded in a carbon layer and (b) Pt (111) surface. In the figure, the gray, blue, yellow, red, white, and silver balls represent C, N, Fe or Mn, O, H, and Pt atoms, respectively. (For interpretation of the references to colour in this figure legend, the reader is referred to the web version of this article.)

$$O_{2(aq)} \leftrightarrow O_{2(dl)} \quad (2)$$

Then O_2 molecule in the double layer may adsorb on the active sites (*) in the catalysts,

$$O_{2(dl)} + * \leftrightarrow {}^*O_2 \quad (3)$$

Once adsorbed on an active site, ${}^*O_2$ can be reduced to form water through a 4 e^- dissociative mechanism (pathway I) involving the direct dissociation of O_2 and several subsequent protonation reactions coupled with electron transfers,

$${}^*O_2 \leftrightarrow {}^*O + {}^*O \quad (4)$$

$${}^*O + {}^*O + H^+ + e^- \leftrightarrow {}^*O + {}^*OH \quad (5)$$

$${}^*O + {}^*O\ H + H^+ + e^- \leftrightarrow {}^*O + H_2O \quad (6)$$

$${}^*O + H^+ + e^- \leftrightarrow {}^*OH \quad (7)$$

$${}^*OH + H^+ + e^- \leftrightarrow H_2\ O + * \quad (8)$$

Alternatively, the reduction reaction can go through a 4 e^- associative mechanism (pathway II) in which ${}^*O_2$ is protonated to form ${}^*OOH$ before dissociation.

$${}^*O_2 + H^+ + e^- \leftrightarrow {}^*OOH \quad (9)$$

$${}^*OOH \leftrightarrow {}^*O + {}^*OH \quad (10)$$

In 4 e^- pathway III, ${}^*OOH$ will be further protonated to ${}^*HOOH$ which dissociates through two possible reactions subsequently.

$${}^*OOH + H^+ + e^- \leftrightarrow {}^*HOOH \quad (11)$$

$${}^*HOOH + * \leftrightarrow {}^*OH + {}^*OH \quad (12)$$

$${}^*HOOH \leftrightarrow {}^*O + H_2O \quad (13)$$

In addition, ${}^*HOOH$ can also desorb from the active sites to produce hydrogen peroxide ending up with a 2 e^- ORR (pathway IV).

$${}^*HOOH \rightarrow * + H_2O_2 \quad (14)$$

For each elementary step (step (2) to (14) above), both the forward and backward reactions have been considered in our model. The forward reaction constant is calculated by the Arrhenius equation

$$k = A \cdot exp(-\frac{E_a(U)}{k_B T}) \quad (15)$$

whereas the backward reaction constant is calculated by

$$k_- = \frac{k}{K} \quad (16)$$

here K is the equilibrium constant, given by

$$K = exp(-\frac{\Delta G(U)}{k_B T}) \quad (17)$$

The pre-exponential factor A and all the other input parameters are given in the supporting information (Table S1). It should be mentioned that the activation energy for the electron transfer coupled protonation reactions is potential dependent and hence calculated using the following equation.

$$E_a(U) = E_a(U_0) + \beta e(U - U_0) \quad (18)$$

In this equation, U_0 is the reversible potential where the reaction free energy is zero, and β is the symmetry factor. The activation energy at the reversible potential $E_a(U_0)$ for each protonation reaction adopts a constant value of 0.26 eV and β adopts a value of 0.5 as suggested in the literature [35].

Derived from the predicted TOF, the potential-dependent current density for the ORR is calculated using Eq. (19).

$$j = e\rho TOF \quad (19)$$

where ρ is the site density. In this way, a polarization curve which reflects the specific activity of the modelled active site for the ORR is attainable from our microkinetic model.

2.3. Mn-N-C Catalyst synthesis and characterization

2.3.1. Catalyst synthesis

To prepare Mn-PANI-hydrogel catalyst, we first dissolved 0.66 g (7.08 mmol) aniline and 0.81 g (3.54 mmol) ammonia persulfate (APS) in 2.0 M hydrochloric acid (HCl) solution (3 mL), respectively, and obtained two samples denoted as Solution A and Solution B. Subsequently, 1.4 g (7.08 mmol) manganese chloride tetrahydrate was dissolved into Solution A. Both solution A and solution B were incubated at 0 °C for 10 min. Then, Solution B (APS solution) was gradually added into Solution A (containing aniline), and the polymerization of aniline was conducted at 0 °C for 10 min. Thus, the gel-like mixture was formed and further aged at room temperature for 24 h. The freeze-drying was used to remove solvent and retain the porous structure of polyaniline hydrogel composite. The resulting gel-like solid (without any grinding) was pyrolyzed at 950 °C for 1 h under nitrogen (N_2) flow with a ramping rate of 3 °C/min. The pyrolyzed solid powder was treated with 0.5 M H_2SO_4 at 80 °C for 5 h and then dried at 60 °C for 12 h, followed by a second pyrolysis at 900 °C for 3 h under N_2 flow with a ramping rate of 3 °C/min.

2.3.2. Physical characterization

Scanning electron microscopy (SEM) images were recorded on a Hitachi SU 70 microscope at a working voltage of 5 kV. Transmission electron microscopy (TEM) was conducted on a JEOL 2100 F and an aberration-corrected Hitachi 2700C scanning transmission electron microscope (STEM) at a voltage of 200 kV. X-ray photoelectron spectroscopy (XPS) was performed using a Kratos AXIS Ultra DLD, equipped with a hemispherical energy analyzer, a monochromatic Al Kα source operated at 15 keV and 150 W, and with pass energy fixed at 40 eV for high-resolution scans. All the samples for XPS measurements were prepared as pressed powders supported on a metal bar. The full width at half maximum (FWHM) of the major XPS peaks range from 0.3 to 1.7 eV for various elements. All the instrument parameters are constant including FWHMs, peak shapes, instrument design factors, chemical shifts, experimental settings and sample factors. The binding energy of Au was used as the reference for calibration.

2.3.3. Electrochemical measurements

Electrochemical measurements were performed on a CHI Electrochemical Station (Model 760b) equipped with high-speed rotators from Pine Instruments. A rotating ring disk electrode (RRDE), which is from Pine Research Instrumental (model: AFE7R9GCPT, USA), was used as the working electrode. It contains glassy carbon disk and platinum ring: disk OD = 5.61 mm; ring OD = 7.92 mm; ID = 6.25 mm; a graphite rod with a diameter of 0.250 inch, a length of 12 inch, and an $Hg/HgSO_4$ as the counter electrode and reference electrode, respectively. Catalyst powder (10 mg) and 5 wt% Nafion® solution (15 µl) were mixed with 1.0 mL isopropanol, and the resulting mixture was then sonicated vigorously for 30 min to obtain a homogeneous ink. The ink was drop-casted onto the glassy carbon disk with 15-min air-drying at 60 °C. The loading of the catalysts for all the measurements was maintained at 0.8 mg/cm^2. All the cyclic voltammetry (CV) and ORR polarization curves were recorded in 0.5 M H_2SO_4. The ORR activity was measured in 0.5 M H_2SO_4 saturated with O_2 at 900 rpm using steady-state polarization plots by holding each potential for 30 s with a potential step of 30 mV. As ORR is a kinetically slow electrochemical reaction, the designed steady-state measurements are to allow the non-faradaic capacitance current passing through and thus accurate measure of the cathodic current exclusively resulting from the ORR. Durability of all the catalysts was assessed in O_2 saturated 0.5 M H_2SO_4 solution using a potential cycling window ranging from 0.6 to

1.0 V at the scanning rate of 50 mV/s.

3. Results and discussion

3.1. Reaction energy calculations

First, we predicted the free energy changes and activation energies for the elementary reactions of ORR on MnN_4, FeN_4 active sites and Pt (111) using the DFT calculations with the explicit solvation (i.e., one water layer above the catalyst surface). One water layer was found sufficient to stabilize the adsorbed ORR intermediates and describe the solvation effect [36,37]. The adsorption configurations of ORR species (including O_2, OOH, O, OH, HOOH, and H_2O) on the active sites were optimized using the RPBE functional (shown Figure S1). The lowest-energy adsorption configuration of O_2 on MnN_4 is that the O_2 molecule lies in parallel to the catalyst layer (denoted as side-on adsorption), resulting in the equal distances between the two O and central Mn atoms. In contrast, the lowest-energy adsorption configuration of O_2 on FeN_4 is that one O atom of the O_2 molecule lies directly on top of central Fe atom whereas the other O atom tilts further away (denoted as end-on adsorption), resulting in the unequal distances between the two O and central Fe atoms. The other species (OOH, O, OH, HOOH, and H_2O) are all adsorbed with one O atom on top of the Mn or Fe and adopting the same adsorption configurations on both FeN_4 and MnN_4. It should be noted that the predicted most favorable adsorption configurations for the ORR species on FeN_4 with an explicit water layer in this work are quite similar to those predicted previously on FeN_4 without considering water environment [38]. However, we noticed that the peripheral water molecules are reorganized to form hydrogen bonds with the adsorbed ORR species, causing the O—O, O—H or M—O bonds (M═Mn or Fe) of the adsorbed ORR species elongated by 1–2 %. In addition to the central Mn and Fe metal sites, we predicted that O and OH could be adsorbed on the carbon atom adjacent to N but with relatively weaker binding strength. Furthermore, we determined the initial, final states of the ORR elementary reactions on the active sites based on our optimized adsorption configurations and used Eq. (1) to calculate the free energy changes (ΔG(U)) for these ORR elementary reactions, which are given in Table S1 of the Supplementary Materials.

Subsequently, we applied the CI-NEB method [32] to locate the transition state and predict the activation energies for O—O bond scission (through direct O_2 dissociation, OOH dissociation, and HOOH dissociation) on MnN_4, FeN_4 sites and Pt (111) using the explicit solvation model. It notes that these O—O bond scission reactions do not involve charge transfer. As a representative case, we depicted in Fig. 2 the atomistic structures of the OOH dissociation reaction pathways on the three catalysts. The OOH dissociation on MnN_4 was predicted to be able to complete on the central Mn atom, with the dissociated O leaning toward a chelated N site whereas the dissociated OH leaning toward adjacent C sites. However, the OOH dissociation on FeN_4 involves a step of the OH transferring to the top of an adjacent carbon atom. In contrast, the OOH adsorbed on a bridge site of Pt (111) with a side-on adsorption configuration was predicted to dissociate into a O and OH adsorbed on two adjacent fcc surface sites (i.e., an fcc surface site is the center of the triangle formed by three neighboring surface atoms and having no atom right beneath in the subsurface layer). Moreover, the atomic details of direct O_2 dissociation and HOOH dissociation on MnN_4, FeN_4, and Pt (111) are shown in Figure S2 of the Supplementary Materials. In these DFT calculations considering explicit water, we predict that the O—O bond breaking process involves at least two adjacent fcc sites on Pt (111), a Fe site and an adjacent carbon site on FeN_4 site, but only a Mn site on MnN_4. We believe that the discrepancy in the OOH dissociation pathway on MnN_4 and FeN_4 is related to the different favorable O_2 adsorption configurations (side-on adsorption on MnN_4 vs. end-on adsorption on FeN_4) on these two sites.

Our predicted activation energies for the O—O bond breaking reactions (i.e., the energy difference between the transition state and the initial state) are presented in Table 1. In the explicit solvation environment, our DFT calculations predict that the activation energy for the O_2 dissociation is 0.85 eV, which is more than two times higher than that (only 0.38 eV) for the OOH dissociation on the MnN_4 site. For the FeN_4 site, we predict a rather high value (2.11 eV) for the activation energy of the O_2 dissociation using the explicit solvation model. It notes that this value is higher than our predicted value (1.19 eV) for the same reaction in vacuum [21]. Despite of discrepancy, these two values are appreciably larger than the activation energy for the OOH dissociation (0.42 eV) on the FeN_4 site and both to the degree of insurmountable. Consequently, it is inferred from our computational results that the OOH dissociation reaction is kinetically more feasible than the O_2 dissociation reaction for the O—O bond breaking on MnN_4 and FeN_4. In comparison, we predict that the activation energy for the OOH dissociation is 0 eV on Pt (111) in explicit water environment.

3.2. Reaction pathways predicted from DFT calculations

Fig. 3 depicts the free energy evolution for the $4e^-$ ORR associative mechanism (*i.e.*, pathway II described in Sec. 2.2) on MnN_4, FeN_4, and

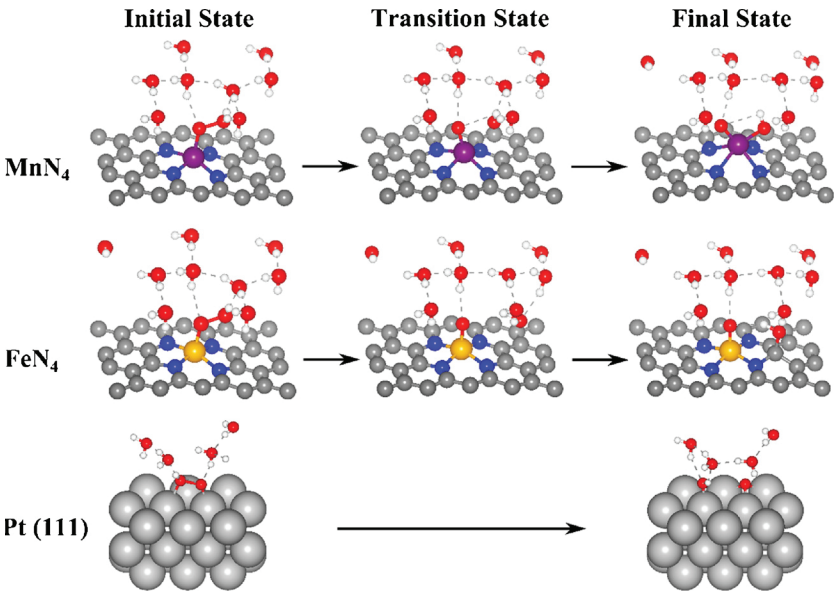

Fig. 2. Atomic structures of the initial state, transition state, and final state for OOH dissociation reaction on MnN_4, FeN_4, and Pt (111) using the explicit solvation model. In the figure, the gray, blue, purple, orange, red, white, and silver balls represent C, N, Mn, Fe, O, H, and Pt atoms, respectively. (For interpretation of the references to colour in this figure legend, the reader is referred to the web version of this article.)

Table 1
Predicted activation energies for O—O bond scission through O_2 dissociation, OOH dissociation, and HOOH dissociation reactions on MnN_4, FeN_4, and Pt (111) surface.

$E_a(eV)$	MnN_4	FeN_4	Pt (111)
$O_2 \rightarrow O+ O$	0.85	2.11	0.44
$OOH \rightarrow O+ OH$	0.38	0.42	0
$HOOH \rightarrow OH+ OH$	–	0	0.07
$HOOH \rightarrow O+ H_2O$	0	0	–

Pt (111) based on the results from the explicit solvation model DFT calculations. The free energy change (ΔG(U)) for the elementary reactions were computed using Eq. (1) and the computational hydrogen electrode method developed by Nørskov et al. [33] In this figure, we include a step of OOH dissociation into O and OH, which does not involve electron transfer and thus is assumed to have a free energy change and activation energy independent of electrode potential (U). All the other electrochemical steps involve proton and electron transfer and hence their free energy change and activation energy are dependent on electrode potential (U).

Fig. 3a shows that, under the standard potentials of the ORR U = 1.23 V, i.e. zero overpotential, most of the elementary reactions along the $4e^-$ ORR associative pathway are endergonic and thus thermodynamically unfavorable on MnN_4, FeN_4, and Pt (111). Associated with the very postitive free energy changes, the required activation energies for the protonation steps are also quite high. For instance, the free energy change for the O protonation reaction to form OH was calculated to be 0.55 eV on MnN_4 and hence its activation energy was predicted to be 0.55 eV according to Eq. (18). Thus, the ORR would be rather difficult to occur under U = 1.23 V on MnN_4, FeN_4, and Pt (111). However, with a decrease in the applied electrode potential U, the free energy changes of the protonation reactions involving charge-transfer decrease and will become negtaive values (*i.e.*, exergonic reaction) below a limiting electrode potential. Based on Eq. (18), the activation energies of these reactions involving charge-transfer would also decrease with decreasing U. For example, the free energy change for the O protonation reaction on MnN_4 was found to change from 0.55 eV (U = 1.23 V) to -0.09 eV (U = 0.58 V). Correspondingly, the activation energy for the same reaction was predicted to decrease from 0.55 eV (U = 1.23 V) to 0.22 eV (U = 0.58 V). Fig. 3b shows that, under a limiting electrode potential U of 0.58 V, all the elementary steps except for the OH protonation reaction along the associative pathway of ORR are exergonic on FeN_4. However, above U = 0.58 V, the OH protonation reaction becomes endergonic on FeN_4. Fig. 3b also shows that, under electrode potential U of 0.58 V, the free energy change for the OH protonation reaction on MnN_4 requires is about 0.05 eV. Consequently, the limiting electrode potetial for the $4e^-$ ORR associative pathway on MnN_4 is predicted to be 0.53 V. At U = 0.58 V (Fig. 3b), we predict that the highest activation energy for all the elementary reactions along the $4e^-$ ORR associative pathway is 0.38 eV for the OOH dissociation reaction on MnN_4, 0.42 eV for OOH dissociation reaction on FeN_4, and 0.43 eV for the O protonation reaction on Pt (111). These activation energies are kinetically surmountable. Thus, we predict that the 4e- associative pathway of ORR is thermodynamically favorable and kinetically feasible on MnN_4, FeN_4, and Pt (111) under U below the limiting electrode potential.

On the other hand, the calcualtion results indicate that it is quite difficult for OOH to be protonated to form HOOH on MnN_4 and FeN_4 sites. It was found that the free energy change for OOH protonation reaction was as high as 0.91 and 1.03 eV on MnN_4 and FeN_4, respectively, under electrode potential of 0.58 V. In comparison, our DFT reulsts in Table 1 suggest that the OOH adsorbed on MnN_4 and FeN_4 could proceed with the dissociation reaction overcoming a relatively low activation energy barrier. In addition to unfavorable protonation of OOH to form HOOH, the HOOH dissociation (either into two hydroxyls, or into one oxygen atom and a water molecule) requires no or very low activation energy on MnN_4, FeN_4, and Pt (111). Consequently, we predict that hydrogen peroxide could not be a stable product of the ORR on these three catalysts. Namely, similar to that on Pt (111), the two-electron ORR pathway to generate hydrogen peroxide as reaction final product is suppressed on both MnN_4 and FeN_4.

Therefore, we predict that ORR would prefer to follow a $4e^-$ associative pathway (i.e., pathway II described in Sec. 2.2) on MnN_4, FeN_4, and Pt (111). Many electrochemical measurements have confirmed $4e^-$ ORR on the Fe-N-C and Pt catalysts, agreeing with our present predictions [4,6,9,39,40]. Our theoretical calculations in Table 1 and Fig. 3 show that the reaction energies for the ORR on MnN_4 are comparable to those on FeN_4, and Pt (111). In theory, the Mn-N-C catalysts containing the MnN_4 sites will promote the 4e- ORR in a fashion comparable to the established Fe-N-C and Pt catalysts.

3.3. Prediction from Microkinetic Analysis

In order to enable direct experimental validation of our computational predictions, we have performed a microkinetic analysis on the kinetic rate of ORR using the reaction energies ($\Delta G(U)$ and $E_a(U)$) on the MnN_4, FeN_4, and Pt (111) sites calculated from the explicit solvation DFT calculations. The details of our employed microkinetic analysis method have been given in Sec. 2.2. As described, the total reaction rate, in term of turnover frequency and current density, for the ORR on various catalysts can be predicted. In this study, we carried out

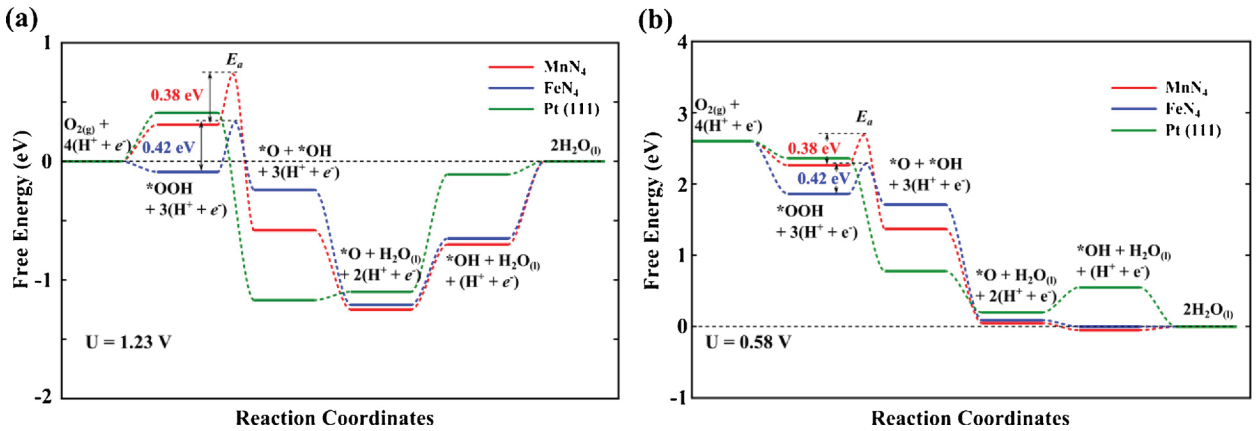

Fig. 3. Predicted free energy evolution diagrams for O_2 reduction through $4e^-$ associative pathway to form H_2O on MnN_4, FeN_4, and Pt (111) surface under electrode potential of (a) U = 1.23 V and (b) U = 0.58 V. The DFT calculations have included the explicit water solvation effect; the free energy calculations are performed at temperature of 300 K and in acid medium with pH value of 0.

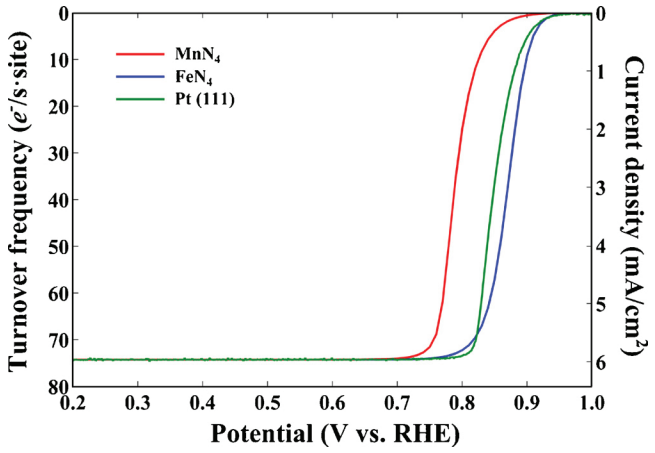

Fig. 4. Polarization curves for ORR on MnN_4, FeN_4, and Pt (111) predicted from our microkinetic analysis and corrected with the experimental data for Pt catalysts.

our microkinetic analysis for the Mn-N-C, Fe-N-C, and Pt catalysts at a temperature of 300 K (27 °C) and in an acid electrolyte with pH value of 0. In addition, we have used the same value of $80.3\,\mu C/cm^2$ for $e\rho$ (note: $e\rho$ is directly related to active site density in Eq. (19)) for the three catalysts. This value was calculated by assuming 1/3 ML (mono-layer) coverage for the Pt (111) surface [34].

We are aware that the real active site density accessible for ORR will vary appreciably with different catalyst morphology and physical properties depending on synthesis processes of actual catalysts. Hence, our present study aims to provide only a qualitative, but not a quantitative, comparison between the computational predictions and electrochemical measurements. Moreover, our microkinetic analysis derived that the half-wave potential for the ORR on Pt (111) surface was about 0.66 V, which differs from the experimental value of 0.85 V [41] by 0.19 V. This discrepancy implies that there could be some systematic error in our computational approach. However, this error should have similar effects on the MnN_4, FeN_4, and Pt (111) catalysts and hence should not affect the relative difference in the activity of the three catalysts. Therefore, we present in Fig. 4 the computed polarization curves, showing the variation of the turnover frequency and the corresponding current density as a function of the electrode potential, for ORR on the MnN_4, FeN_4, and Pt (111) with the same active site density, with a correction by up-shifting the three curves by 0.19 V.

Shown in Fig. 4, we predict that the half-wave potential for ORR on FeN_4 to be even higher by 0.02 V than that on Pt (111) if the two catalysts have the same density of active sites. Recent development of the Fe-N-C catalysts yielded catalytic activity for the ORR very close to that of Pt in acids [5,9], which is in good agreement with our present computational predictions. Moreover, we predict from Fig. 4 that the MnN_4 site could exhibit a half-wave potential for ORR only 60 mV lower than that of Pt (111) and 80 mV lower than that of the FeN_4. It was thus inferred that the well-synthesized Mn-N-C catalysts could possess an ORR activity close to that of the Fe-N-C catalysts.

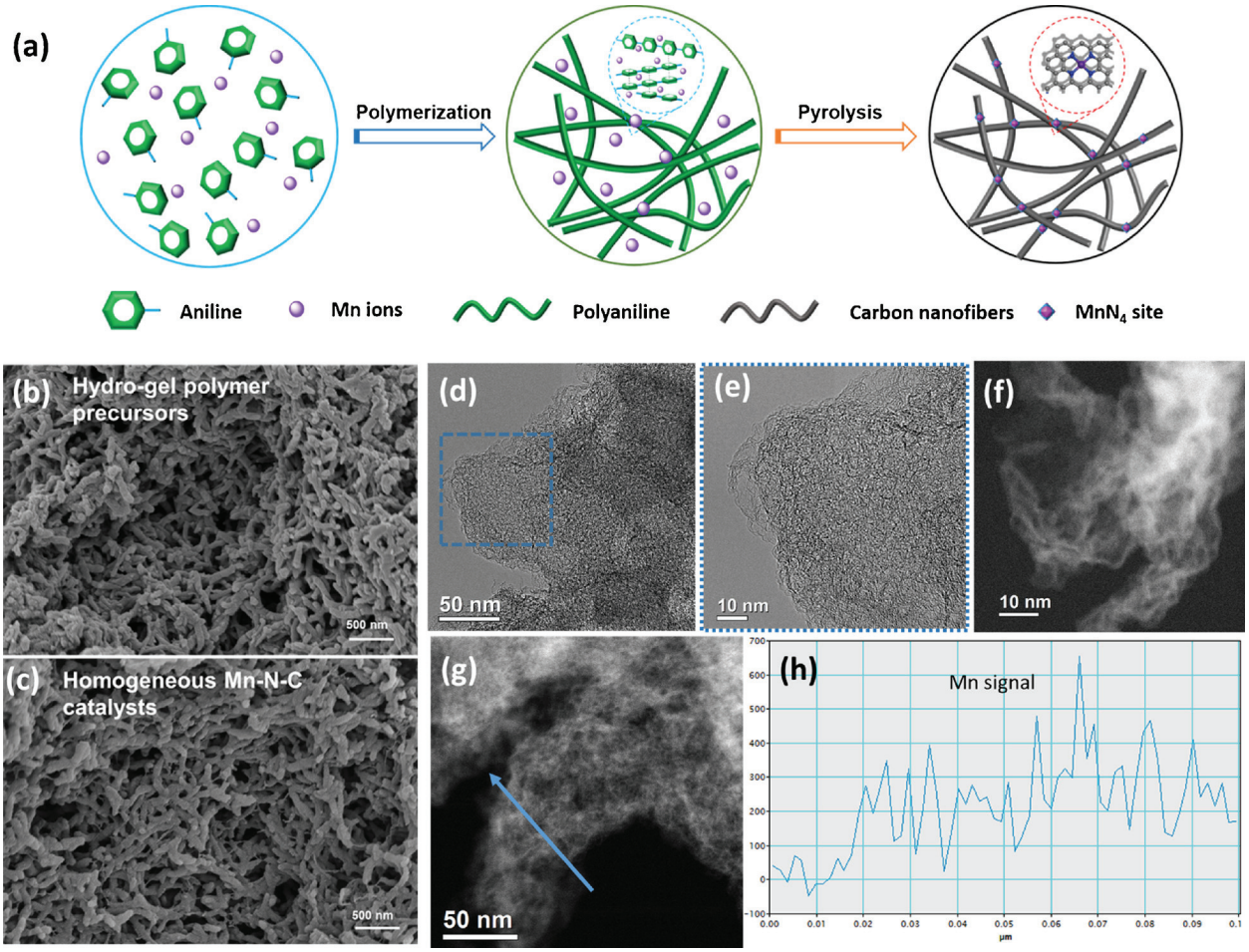

Fig. 5. (a) Synthesis scheme for the Mn-N-C catalysts produced by PANI-hydrogel approach. SEM images showing the morphology of (b) the PANI-hydrogel precursor and (c) the Mn-N-C catalyst during a carbonization process. (d, e) HR-TEM and (f, g) HAADF-STEM images coupled with (h) EELS analysis of the Mn-N-C catalyst, indicating partially graphitized and nanoporous morphology likely with atomically dispersed Mn sites.

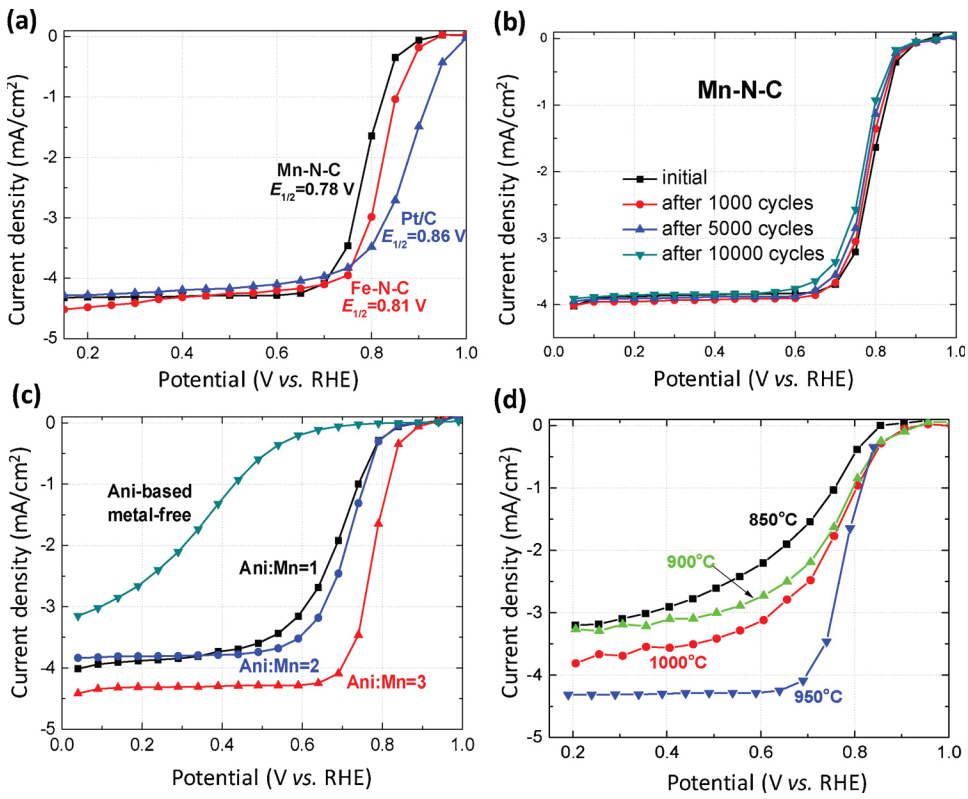

Fig. 6. (a) Comparison of steady-state ORR polarization plots recorded in 0.5 M H_2SO_4 of the Mn-N-C and Fe-N-C catalysts prepared from the PANI hydrogel approach, and a 20 wt % Pt/C catalyst at a loading of 60 $\mu g_{Pt}/cm^2$. (b) Potential cyclic stability of the Mn-N-C catalysts between 0.6-1.0 V in O_2 saturated 0.5 M H_2SO_4. The variation in the ORR activity of PANI hydrogel-derived Mn-N-C catalysts as a function of the (c) Mn content and (d) pyrolysis temperature. Catalyst loading for all the tests is 0.8 mg/cm^2 at 900 rpm and 25 °C.

Furthermore, our microkinetic analysis confirms the occurring of $4e^-$ ORR on MnN_4 sites. The calculation results reveal that the $4e^-$ ORR associative pathway (i.e., pathway II described in Sec. 2.2 and shown in Fig. 3) is dominantly active on the MnN_4 up to U = 0.75 V, whereas the $4e^-$ ORR dissociative pathway through direct O_2 dissociation (*i.e.*, pathway I described in Sec. 2.2) is dominantly active on the MnN_4 above U = 0.75 V. This change in reaction pathway is because that the activation energy for the O_2 protonation reaction on the MnN_4 would increase with electrode potential U and at U = 0.75 V leading to a net reaction rate comparable to that of the O_2 dissociation on the MnN_4. As shown in Figure S3 of Supplementary Materials, our microkinetic analysis also reveals that surface adsorbed OH, O_2, and O would accumulate on the MnN_4 sites and reach their maximum coverage at the electrode potential (U) around 0.55 V, 0.62 V, and 0.82 V, respectively. The accumulation of these surface species will hinder the ORR on the MnN_4. Hence, our present study suggests that development of effective approaches to remove these surface species from the MnN_4 sites could be a practical way to further enhance the ORR activity of Mn-N-C catalysts.

3.4. Experimental Validation

Inspired by the computational prediction, we have developed a polymer hydrogel approach to preparing Mn-N-C catalysts. The synthesis scheme is illustrated in Fig. 5a. We used polyaniline (PANI) as carbon/nitrogen sources integrated with metal precursors to produce the highly active M-N-C catalysts for the ORR through a high-temperature approach [4]. Distinct from traditional carbon black (*e.g.*, Ketjenblack or Blackpear) supported PANI-derived catalysts, self-standing and support-free PANI hydrogels were used in this work by properly controlling the high concentration of aniline in solution and being polymerized using ammonium persulfate as the oxidizing agent. Mn^{2+} sources were added during the polymerization process and uniformly dispersed into the PANI hydrogel precursors. A high temperature carbonization process was employed to convert the PANI-Mn hydrogel into Mn and N co-doped carbon, *i.e.* the Mn-N-C catalysts. Subsequent acid-leaching treatment followed by a second pyrolysis process was carried out to remove inactive species and recover oxidized carbon for enhanced catalytic activity.

SEM images (Fig. 5b and c) show that the three-dimensional (3D) cross-linked network porous fiber morphology of the PANI hydrogels was largely maintained in the final Mn-N-C catalysts after high temperature pyrolysis process. It is also believed that this highly porous carbon structure is of vital importance for uniformly dispersing active sites in the carbon to achieve high activity and stability. Further high resolution (HR)-TEM images (Fig. 5d and e) and high angle annular dark field (HAADF)-STEM images (Fig. 5f and g) provide the detailed morphology of the catalysts. Overall, highly disordered or even amorphous carbon structures are dominant in the catalyst. Virtually, no obvious metallic particles or aggregates are observable. The electron energy-loss spectroscopy (EELS) line scanning (Fig. 5h) was conducted in the area marked in Fig. 5g, showing significant Mn signal. This elemental analysis suggests that the existence of atomically dispersed Mn sites is very likely in the PANI-hydrogel derived Mn-N-C catalysts. We believe that such atomic metal sites could be stablized by Mn ions coordination with nitrogen and embedded into carbon layers.

Moreover, the role of crucial nitrogen doping was further investigated using XPS. Figure S4 indicates that the nitrogen doping in the catalyst is greatly dependent on the content of Mn used for catalyst synthesis. High Mn content leads to high concentration of pyridinc N and total N. It was inferred that high content of pyridinic N was able to enhance the density of active sites for the M-N-C catalysts. In addition, pyrolysis temperature used for carbonization of the PANI hydrogel is vital for the formation of active sites, which was further linked to nitrogen doping (Figure S5a). However, our XPS analysis indicated that the surface Mn content maintained at 0.4 at.% ~ 0.5 at.% for all these catalyst samples shown in Figure S5a, thus showing little dependence on the pyrolysis temperature. In comparison, the typical Fe concentration is about 0.8 at.% in Fe-N-C samples. When the pyrolysis temperature is above 950 °C, the resultant catalysts contain higher content of pyridinic N, which could lead to enhanced ORR activity (Figure S5b) [42]. Unlike previous results for the synthesis of Fe- and

Co-based catalysts [43,44], high pyrolysis temperature for the Mn catalysts leads to increased nitrogen content and pyridinic nitrogen (Figure S5b). High pyrolysis temperature also results in a high degree of graphitization in the catalysts. Figure S6 also indicates that our synthesized Mn-N-C catalyst shows relatively narrow peak for C-C than that of the Fe-N-C catalysts just owing to its high degree of graphitization [45–47]. It is believed that graphitized carbon would have beneficial effect on the stability of the Mn-N-C catalysts.

In this study, our experimental validation confirms the computational prediction and shows that the PANI hydrogel-derived Mn-N-C catalyst exhibited ORR activity comparable to that of the Fe-N-C catalyst prepared using the same synthesis approach in 0.5 M H_2SO_4 electrolyte (Fig. 6a). The ORR on the Mn-N-C catalyst occurs nearly via four-electron pathways, as evidenced by very low H_2O_2 yields (< 3%,) as shown in Figure S7 [21,48,49]. Although the half-wave potential of the Mn-N-C is 0.78 V *vs.* RHE slightly lower than that of the Fe-N-C catalyst (0.80 V), their onset potentials are nearly the same indicating similar intrinsic activity to catalyze the ORR. We attribute the 20 mV difference in the half-wave potentials of the Mn-N-C and Fe-N-C to the relatively low specific activity and surface density of the MnN_4 active sites in our catalysts. In addition, the comparsion with commerical Pt/C was also given in Figure S8. Importantly, the Mn-N-C catalyst demonstrated superior potential cyclic stability, only losing 20 mV after 10000 cycles (0.6 to 1.0 V in O_2 saturated electrolyte) (Fig. 6b). Under the identical testing conditions, the Fe-N-C catalyst would loss 80 mV after 5000 cycles (Figure S9). During the synthesis, we identified two key factors crucial for optimizing the ORR activity of the Mn-N-C catalysts: (1) the Mn content integrated with PANI hydrogel (Fig. 6c) and (2) the pyrolysis temperature (Fig. 6d), which can be explained by optimal nitrogen doping and favorable catalyst morphologies as shown in Figure S4 to S6. Although we do not have conclusive evidence to show the existence of exact MnN_4 site structure in the catalyst, it can be inferred from the HAADF-STEM images coupled with EELS analysis (Fig. 5g and h) that the existence of atomically dispersed Mn coordinated with nitrogen is very likely in the catalysts. Thus, our present experimental results, which the Mn-N-C catalysts possess good ORR activity and stability in acid media, provide a solid validation to the computational prediction of the ORR activity on the MnN_4 sites.

4. Conclusions

In summary, we have performed the first-principles DFT calculations and the microkinetic analysis to predict the catalytic activity of the MnN_4 active site embedded in a carbon layer for the ORR in acids. Taking solvation effect into account, we included a monolayer of water molecules above the catalyst surface in our DFT calculations. Our DFT calculation results indicate that the MnN_4 site can catalyze the ORR following a $4e^-$ pathway, which has a thermodynamical limiting electrode potential of 0.53 V and the highest activation energy of only 0.38 eV for the OOH dissociation reaction. Based on the reaction energies calculated from DFT, our microkinetic analysis predicted the polarization curves for ORR on the electrocatalysts containing the same density of MnN_4, FeN_4, or Pt (111) active sites. The results reveal that the MnN_4 sites could catalyze ORR with a half-wave potential only 60 mV lower than that of Pt (111) sites and 80 mV lower than that of the FeN_4 sites. Therefore, our computational study suggests that the Mn, N co-doped carbon containing the MnN_4 active sites should exhibit promising high-performance to catalyze ORR in acid electrolytes. To validate our computational predictions, we have further carried out experimental study to synthesize Mn-N-C catalysts through an innovative polyaniline hydrogel approach. The ORR activity of the Mn-N-C catalyst measured using RRDE is comparable to that of the Fe-N-C catalyst prepared from the same synthesis procedures, which verifies our computational prediction. Physical characterization further indicates that the atomically dispersed Mn sites coordinated with N very likely exist in our synthesized Mn-N-C catalysts. More encouragingly, durability tests show that the Mn-N-C catalysts exhibit enhanced stability than the Fe-N-C catalysts under the same electrochemical testing conditions.

The combined computational and experimental studies reveal that the Mn-N-C catalysts containing planar MnN_4 sites embedded in carbon layer could exhibit comparable ORR activity and enhanced durability relative to the conventional Fe-N-C catalysts. The findings from this work may provide knowledge for the rational design and synthesis of PGM-free and Fe-free electrocatalysts for PEMFCs. Future research will focus on the ultimate verification of existence of the MnN_4–like active sites and further improvement of ORR performance of the Mn-N-C catalysts by generating increased density of active sites.

Acknowledgments

This research was financially supported by Office of Energy Efficiency and Renewable Energy, U.S. Department of Energy (Grant no. DE-EE0008075). G.F. Wang also acknowledges the research grants from National Science Foundation (Grant No. CBET-1804534 and CMMI-1662615). G. Wu also thanks the financial support from National Science Foundation (CBET- 1604392). The authors gratefully acknowledge the computational resources provided by the University of Pittsburgh Center for Research Computing as well as the Extreme Science and Engineering Discovery Environment (XSEDE), which is supported by National Science Foundation grant number ACI-1053575.

Appendix A. Supplementary data

Supplementary material related to this article can be found, in the online version, at doi:https://doi.org/10.1016/j.apcatb.2018.10.034.

References

[1] R.A. Lemons, Fuel-cells for transportation, J. Power Sources 29 (1990) 251–264.
[2] M.K. Debe, Electrocatalyst approaches and challenges for automotive fuel cells, Nature 486 (2012) 43–51.
[3] M. Lefèvre, E. Proietti, F. Jaouen, J.P. Dodelet, Iron-based catalysts with improved oxygen reduction activity in polymer electrolyte fuel cells, Science 324 (2009) 71–74.
[4] G. Wu, K.L. More, C.M. Johnston, P. Zelenay, High-performance electrocatalysts for oxygen reduction derived from Polyaniline, Iron, and cobalt, Science 332 (2011) 443–447.
[5] H.G. Zhang, H. Osgood, X.H. Xie, Y.Y. Shao, G. Wu, Engineering nanostructures of PGM-free oxygen-reduction catalysts using metal-organic frameworks, Nano Energy 31 (2017) 331–350.
[6] S. Gupta, S. Zhao, O. Ogoke, Y. Lin, H. Xu, G. Wu, Engineering favorable morphology and structure of Fe-N-C oxygen-reduction catalysts through tuning of Nitrogen/Carbon precursors, Chemsuschem 10 (2017) 774–785.
[7] H.L. Peng, F.F. Liu, X.J. Liu, S.J. Liao, C.H. You, X.L. Tian, H.X. Nan, F. Luo, H.Y. Song, Z.Y. Fu, P.Y. Huang, Effect of transition metals on the structure and performance of the doped carbon catalysts derived from polyaniline and melamine for ORR application, ACS Catal. 4 (2014) 3797–3805.
[8] X.J. Wang, H.G. Zhang, H.H. Lin, S. Gupta, C. Wang, Z.X. Tao, H. Fu, T. Wang, J. Zheng, G. Wu, X.G. Li, Directly converting Fe-doped metal organic frameworks into highly active and stable Fe-N-C catalysts for oxygen reduction in acid, Nano Energy 25 (2016) 110–119.
[9] H. Zhang, S. Hwang, M. Wang, Z. Feng, S. Karakalos, L. Luo, Z. Qiao, X. Xie, C. Wang, D. Su, Y. Shao, G. Wu, Single atomic Iron catalysts for oxygen reduction in acidic media: particle size control and thermal activation, J. Am. Chem. Soc. 139 (2017) 14143–14149.
[10] Z. Qiao, H. Zhang, S. Karakalos, S. Hwang, J. Xue, M. Chen, D. Su, G. Wu, 3D polymer hydrogel for high-performance atomic iron-rich catalysts for oxygen reduction in acidic media, Appl. Catal. B-Environ. 219 (2017) 629–639.
[11] J. Tian, A. Morozan, M.T. Sougrati, M. Lefèvre, R. Chenitz, J.P. Dodelet, D. Jones, F. Jaouen, Optimized synthesis of Fe/N/C cathode catalysts for PEM fuel cells: a matter of iron-ligand coordination strength, Angew. Chemie Int. Ed. English 52 (2013) 6867–6870.
[12] X.D. Yang, Y.P. Zheng, J. Yang, W. Shi, J.H. Zhong, C.K. Zhang, X. Zhang, Y.H. Hong, X.X. Peng, Z.Y. Zhou, S.G. Sun, Modeling Fe/N/C catalysts in monolayer graphene, ACS Catal. 7 (2017) 139–145.
[13] V. Armel, S. Hindocha, F. Salles, S. Bennett, D. Jones, F. Jaouen, Structural descriptors of zeolitic-imidazolate frameworks are keys to the activity of Fe-N-C catalysts, J. Am. Chem. Soc. 139 (2017) 453–464.
[14] A. Zitolo, V. Goellner, V. Armel, M.T. Sougrati, T. Mineva, L. Stievano, E. Fonda, F. Jaouen, Identification of catalytic sites for oxygen reduction in Iron- and

nitrogen-doped graphene materials, Nat. Mater. 14 (2015) 937–942.
[15] H.T. Chung, D.A. Cullen, D. Higgins, B.T. Sneed, E.F. Holby, K.L. More, P. Zelenay, Direct atomic-level insight into the active sites of a high-performance PGM-Free ORR catalyst, Science 357 (2017) 479–483.
[16] J. Liu, E.L. Li, M.B. Ruan, P. Song, W.L. Xu, Recent progress on Fe/N/C electrocatalysts for the oxygen reduction reaction in fuel cells, Catalysts 5 (2015) 1167–1192.
[17] M. Ferrandon, X.P. Wang, A.J. Kropf, D.J. Myers, G. Wu, C.M. Johnston, P. Zelenay, Stability of Iron species in heat-treated polyaniline-iron-Carbon polymer electrolyte fuel cell cathode catalysts, Electrochim. Acta 110 (2013) 282–291.
[18] G. Wu, K. Artyushkovab, M. Ferrandonc, J. Kropfc, D. Myersc, P. Zelenay, Performance durability of polyaniline-derived non-precious cathode catalysts, ECS Trans. 25 (2009) 1299–1311.
[19] D. Banham, S. Ye, K. Pei, J. Ozaki, T. Kishimoto, Y. Imashiro, A review of the stability and durability of non-precious metal catalysts for the oxygen reduction reaction in proton exchange membrane fuel cells, J. Power Sources 285 (2015) 334–348.
[20] X. Wang, D. Cullen, Y. Pan, S. Hwang, M. Wang, Z. Feng, J. Wang, M. Engelhard, H. Zhang, Y. Shao, D. Su, K. More, J. Spendelow, G. Wu, Nitrogen coordinated single cobalt atom catalysts for oxygen reduction in proton exchange membrane fuel cells, Adv. Mater. 30 (2018) 1706758.
[21] K.X. Liu, S. Kattel, V. Mao, G.F. Wang, Electrochemical and computational study of oxygen reduction reaction on nonprecious transition Metal/Nitrogen doped carbon nanofibers in acid medium, J. Phys. Chem. C 120 (2016) 1586–1596.
[22] Y. Zheng, D.S. Yang, J.M. Kweun, C. Li, K. Tan, F.T. Kong, C.P. Liang, Y.J. Chabal, Y.Y. Kim, M. Cho, J.S. Yu, K. Cho, Rational design of common transition metal-nitrogen-Carbon catalysts for oxygen reduction reaction in fuel cells, Nano Energy 30 (2016) 443–449.
[23] W. Kohn, L.J. Sham, Self-consistent equations including exchange and correlation effects, Phys. Rev. 140 (1965) A1133–A1138.
[24] P. Hohenberg, W. Kohn, Inhomogeneous Electron gas, Phys. Rev. 136 (1964) B864–B871.
[25] G. Kresse, J. Hafner, Ab initio molecular dynamics for liquid metals, Phys. Rev. B 47 (1993) 558–561.
[26] G. Kresse, J. Furthmuller, Efficiency of ab-initio total energy calculations for metals and semiconductors using a plane-wave basis set, Comput. Mater. Sci. 6 (1996) 15–50.
[27] P.E. Blochl, Projector augmented-wave method, Phys. Rev. B 50 (1994) 17953–17979.
[28] G. Kresse, D. Joubert, From ultrasoft pseudopotentials to the projector augmented-wave method, Phys. Rev. B 59 (1999) 1758–1775.
[29] B. Hammer, L.B. Hansen, J.K. Nørskov, Improved adsorption energetics within density-functional theory using revised perdew-burke-Ernzerhof functionals, Phys. Rev. B 59 (1999) 7413–7421.
[30] H.J. Monkhorst, J.D. Pack, Special points for brillouin-zone integrations, Phys. Rev. B 13 (1976) 5188–5192.
[31] H. Ogasawara, B. Brena, D. Nordlund, M. Nyberg, A. Pelmenschikov, L.G.M. Pettersson, A. Nilsson, Structure and bonding of water on Pt(111), Phys. Rev. Lett. 89 (2002) 276102.
[32] G. Henkelman, B.P. Uberuaga, H. Jonsson, A climbing image nudged elastic band method for finding saddle points and minimum energy paths, J. Chem. Phys. 113 (2000) 9901–9904.
[33] J.K. Nørskov, J. Rossmeisl, A. Logadottir, L. Lindqvist, J.R. Kitchin, T. Bligaard, H. Jonsson, Origin of the overpotential for oxygen reduction at a fuel-cell cathode, J. Phys. Chem. B 108 (2004) 17886–17892.
[34] H.A. Hansen, V. Viswanathan, J.K. Nørskov, Unifying Kinetic and Thermodynamic Analysis of 2 e^- and 4 e^- Reduction of Oxygen on Metal Surfaces, J. Phys. Chem. C 118 (2014) 6706–6718.
[35] V. Tripkovic, E. Skulason, S. Siahrostami, J.K. Norskov, J. Rossmeisl, The oxygen reduction reaction mechanism on Pt(111) from density functional theory calculations, Electrochim. Acta 55 (2010) 7975–7981.
[36] J. Rossmeisl, E. Skulason, M.E. Bjorketun, V. Tripkovic, J.K. Norskov, Modeling the electrified solid-liquid interface, Chem. Phys. Lett. 466 (2008) 68–71.
[37] S.Z. Liu, M.G. White, P. Liu, Mechanism of oxygen reduction reaction on Pt(111) in alkaline solution: importance of chemisorbed water on surface, J. Phys. Chem. C 120 (2016) 15288–15298.
[38] S. Kattel, G. Wang, Reaction pathway for oxygen reduction on FeN_4 embedded graphene, J. Phys. Chem. Lett. 5 (2014) 452–456.
[39] H.A. Gasteiger, S.S. Kocha, B. Sompalli, F.T. Wagner, Activity benchmarks and requirements for Pt, Pt-alloy, and non-Pt oxygen reduction catalysts for PEMFCs, Appl. Catal. B-Environ. 56 (2005) 9–35.
[40] W. Gao, D. Havas, S. Gupta, Q. Pan, N. He, H. Zhang, H.-L. Wang, G. Wu, Is reduced graphene oxide favorable for nonprecious metal oxygen-reduction catalysts? Carbon 102 (2016) 346–356.
[41] J. Greeley, I.E.L. Stephens, A.S. Bondarenko, T.P. Johansson, H.A. Hansen, T.F. Jaramillo, J. Rossmeisl, I. Chorkendorff, J.K. Nørskov, Alloys of platinum and early transition metals as oxygen reduction electrocatalysts, Nat. Chem. 1 (2009) 552–556.
[42] X. Cui, S. Yang, X. Yan, J. Leng, S. Shuang, P.M. Ajayan, Z. Zhang, Pyridinic-nitrogen-Dominated graphene aerogels with Fe–N–C coordination for highly efficient oxygen reduction reaction, Adv. Funct. Mater. 26 (2016) 5708–5717.
[43] G. Wu, N.H. Mack, W. Gao, S. Ma, R. Zhong, J. Han, J.K. Baldwin, P. Zelenay, Nitrogen-doped graphene-rich catalysts derived from heteroatom polymers for oxygen reduction in nonaqueous Lithium–O_2 battery cathodes, ACS Nano 6 (2012) 9764–9776.
[44] Q. Li, P. Xu, W. Gao, S. Ma, G. Zhang, R. Cao, J. Cho, H.L. Wang, G. Wu, Graphene/Graphene-tube nanocomposites templated from cage-containing metal-organic frameworks for oxygen reduction in Li–O_2 batteries, Adv. Mater. 26 (2014) 1378–1386.
[45] H. Estrade-Szwarckopf, XPS photoemission in carbonaceous materials: a “Defect” peak beside the graphitic asymmetric peak, Carbon 42 (2004) 1713–1721.
[46] S. Gupta, S. Zhao, X.X. Wang, S. Hwang, S. Karakalos, S.V. Devaguptapu, S. Mukherjee, D. Su, H. Xu, G. Wu, Quaternary FeCoNiMn-Based nanocarbon electrocatalysts for bifunctional oxygen reduction and evolution: promotional role of Mn doping in stabilizing carbon, ACS Catal. 7 (2017) 8386–8393.
[47] S. Zhao, Zq. Shi, Cy. Wang, Mm. Chen, Structure and surface elemental state analysis of polyimide resin film after carbonization and graphitization, J. Appl. Polym. Sci. 108 (2008) 1852–1856.
[48] R. Zhou, Y. Zheng, M. Jaroniec, S.-Z. Qiao, Determination of the Electron transfer number for the oxygen reduction reaction: from theory to experiment, ACS Catal. 6 (2016) 4720–4728.
[49] K. Chen, M. Wang, G.L. Li, Q.G. He, J. Liu, F.Z. Li, Spherical alpha-MnO2 supported on N-KB as efficient electrocatalyst for oxygen reduction in Al-Air battery, Materials 11 (2018) 601.